

Measurements of liquid film thickness for a droplet at a two-fluid interface

U. Miessner,* E. Coyajee, R. Delfos, R. Lindken, and J. Westerweel

Laboratory for Aero and Hydrodynamics, Leeghwaterstraat 21 2628 CA Delft, The Netherlands

(Dated: June 3, 2019)

The impact of a buoyancy driven oil droplet with an oil-water interface is investigated using time-resolved Particle Image Velocimetry (PIV) along with a phase discrimination by means of high-speed Laser Induced Fluorescence (LIF). In this paper we focus on the investigation of strategies to optimize the performance of high-speed PIV algorithms. Furthermore this data will be used for validation of numerical simulations of two phase flows. In order to simultaneously measure the flow velocities inside and around the oil droplet by means of PIV the refractive indices of both phases need to be carefully matched. The aqueous phase consists of a mixture of corn syrup and water, which defines the viscosity as well as the refractive index. The dispersed phase consists of a mixture of two kinds of mineral oils. The latter are mixed to match the refractive index of the continuous phase. Both phases are seeded with tracer particles required for PIV. A fluorescent dye is added to the dispersed phase to allow discrimination of the PIV signals originating from both phases by means of LIF. The LIF and PIV signals are captured by two aligned, synchronized highspeed cameras, each used for one of the measurement techniques. In order to study the impact of an oil droplet into an oil-water interface, it is necessary to accurately measure a velocity range that is spread over three orders of magnitude. The impact of the droplet is measured in a time series of PIV recordings with a high temporal resolution. This allows to optimize the time interval between two correlated frames within the time series to achieve a high signal-to-noise ratio, while still being able to measure a large velocity dynamic range. An approach to estimate an optimal time separation is presented in this study. The results are compared to the experimental data of Mohamed-Kassim and Longmire [1] and the effectiveness of the introduced optimization on the data quality is discussed. Furthermore the results of this experiment are compared to a numerical simulation developed by Coyajee et al. [2].

INTRODUCTION

A large variety of physical and chemical processes involve two immiscible liquids, e.g. extraction, oil production and transport, emulsification and separation. Understanding of the motion of individual droplets and their interactions is crucial for economically and ecologically optimized design. While the behavior of single droplets is known to a large extent, the interaction of two dispersed droplets (e.g. deformation, break-up, collision and coalescence) is less understood. In the past, several studies have investigated the interaction of droplets and surfaces in order to understand the complex mechanisms involved. A number of studies dealt with the examination of droplets falling through a gas before impacting on a liquid surface. For an overview about PIV experiments in dispersed two-phase flows the reader is referred to [1], [3], [4]. Because of the low viscosity of the surrounding gas the film between the impacting droplet and the surface drains quickly in this case: the droplet immediately coalesces. To study impact without instant merge of the two liquids, a higher viscosity of the surrounding fluid is required to establish a thin film between the surface and the droplet. Coalescence will eventually occur once the film is drained, but it is no longer directly coupled to the impact event. Mohamed-Kassim and Longmire [1] published an experimental study using this approach, focusing their investigation on the hydrodynamics of the liquids involved in the impact. The viscosity ratio chosen

is much closer to unity the ratio realized in this study. The data obtained in this study will provide a more demanding benchmark for numerical simulations. High-speed PIV ([5], [6], [7]) with a frequency of 500 Hz was applied to visualize and quantify the fluid flow. However, it is possible to further increase the accuracy of such measurements with a higher frame rate and a method which allows to adjust the time interval between two correlated particle images to the actual change of flow conditions. In this work the highly instationary flow conditions during a droplet impact are chosen to provide a laminar test case with steep spatial and temporal velocity gradients. Performing measurements in such a flow at very high sample frequencies does not automatically provide better results if consecutive particle images are correlated: the measured displacement, which scales with the delay time between two images, can become so small that they will be of the same order of magnitude as the measurement accuracy of the system.

While the correlation of the particle images [8] may be high (leading to a low percentage of spurious vectors), the result will suffer from a lack in dynamic range and will thus be noisy. Increasing the time separation between two images decreases the signal-to-noise ratio (SNR) but simultaneously increases the velocity dynamic range (VDR). Depending on the flow conditions, each image pair requires an optimal time separation in order to increase the overall accuracy of the investigation. The aim of the present study is to identify parameters which can be utilized to adjust the separation time individually

for each correlation. Additionally, it is our objective to use the data to validate results from numerical simulations. Thus a higher viscosity ratio between continuous and dispersed phase is chosen to provide a demanding test case for numerical simulations. The LIF data is used to detect and track the interfaces between the phases. The experimental results are then compared to numerical results from a simulation performed with the recently developed Mass Conserving Level-Set (MCLS) method [9], [10]. The detailed validation will be topic of a different paper.

EXPERIMENTAL

Facility

A glass tank with a square section of 50 mm width and 600 mm height is used for the investigation of the droplet impact (see Fig. 1). Between nozzle and interface a distance of 100 mm is maintained. The liquid layer on top of the bulk phase has a thickness of 50 mm. The liquids used are a glucose-water mixture (C6H12O6/H2O) for the continuous phase and an oil-oil mixture (Shell Macron EDM 110 / Shell Garia GX 32) for the dispersed phase. Values for the liquid properties are given in table 1. The refractive index of the mixtures is matched to minimize optical distortion with an accuracy of the actual value of 0.03%. Droplet and top layer consist of the same liquid. A more detailed description of the matching procedure is given in section 2.2. A droplet with an equivalent diameter of $D = 11$ mm is generated by injecting the oil mixture into the bulk phase through a cylindrical nozzle of 60 mm length and 5 mm diameter. To ensure that this process is reproducible, the injection is driven by a computer-controlled syringe pump. Tracer particles (Sphericell 110-P-8) are added to both phases. The tracer particles have a nominal diameter of 10 nm to visualize and measure the flow conditions with PIV. Additionally, a fluorescent dye (Hostasol Yellow 3G) is dissolved into the oil mixture in order to discriminate between the two refractive-index-matched liquids. A thin planar light sheet (thickness 1 mm) is formed using a pulsed Nd:YLF laser (527 nm, New Wave Pegasus) in combination with a cylindrical and a spherical lens (focal lengths: $F_c = -80$ mm, $F_s = 350$ mm).

The laser light sheet illuminates a measurement volume in the middle of the tank of approximately 25×50 mm, centered around the impacting droplet. Two high-speed cameras (Photron: Ultima APX-RS, 1024×1024 pixels) are mounted orthogonally to the measurement plane (one on each side, see Fig. 1). They are triggered synchronously with the laser pulses; the laser and cameras are operated at 3000 Hz. A third camera (Sensicam QE) is mounted above the experimental section (Top Cam in Fig. 1) to validate the droplet position relative to

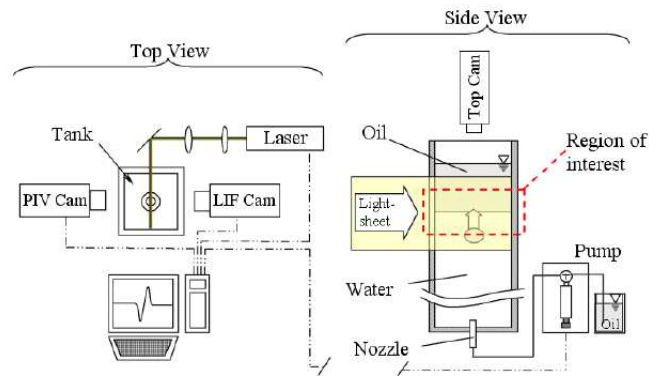


FIG. 1. Schematic representation of the experimental set up showing the top view (left) and the side view (right) of the tank and measurement equipment.

the light sheet [11]. Alignment of the high-speed cameras is done by cross-correlation particle images of camera 1 with camera 2 [12] (both recorded at the same instance). An optical filter (Schott ref.#OG570, $\lambda_{cutoff} = 570 \pm 6$ nm) is mounted in front of camera 2. The orange filter absorbs the light at the original laser wave length (532 nm) and transmits the longer wavelength of the fluorescence. Camera 2 records the scattered light from the tracer particles through a gray filter (B+W Graufilter, neutral density 2). The gray filter is used to reduced the light intensity towards camera 2 in such a way, that the LIF recordings can be illuminated with the same laser pulse of about 100 mJ energy. The syringe pump is coupled to the timing unit of the PIV-system. The data acquisition can be triggered by the droplet injection controller.

The experimental conditions mentioned above are comparable to those reported in [1]. Important differences between both experiments are the restricted domain size and the motion of the impacting droplet (sinking droplets vs. rising droplets in the current study). The reason for the domain restriction is the correspondence to the numerical simulation which is computed in an identical finite domain. Due to symmetry reasons, the opposite droplet motion in the set-up does not have significant effects when the results are compared to the results presented by [1]. A list of physical properties of both investigations is given in table 1. Here U_i is the impact velocity, $t_g = \sqrt{D/(\Delta\rho \cdot g/\rho_{mean})}$ denotes the gravity timescale and $t_i = D/U_i$ is the impact time scale. The Weber number $We = \rho_d U_i^2 / \sigma$, where ρ_d is the density of the droplet, D the droplet diameter and σ the surface tension, and Reynolds number $Re = \rho_s U_{term} D / \mu_s$ use the index s for ambient fluid and d for droplet fluid. The density ratio in Tab. 1 is given as a reciprocal because of the inversed droplet motion. Due to the choice of liquid mixtures the viscosity ratio is much lower than the exper-

iment of [1]. Also a higher Weber number occurs because of the lower surface tension coefficient $\sigma = 0.02N/m$.

TABLE I. Experimental conditions.

	Mohamed-Kassim & Longmire experiment/DNS []			
D	cm	1.03	1.03	1.1
U_i	cm/s	13.2	9.8	25
t_i	ms	78	105	44
t_g	ms	78	80	49
ρ_d/ρ_s	-	1.189	1.178	$(1.625)^{-1}$
μ_d/μ_s	-	0.33	0.14	0.03
Re	-	68	20	36
We	-	7.0	3.8	28
Fr	-	1.0	0.6	0.6

Refractive index matching

PIV measurements are performed inside and outside the impacting droplet. A mismatch of refractive indices would lead to optical distortion due to a lens effect caused by the curvature of the droplet interface. To avoid optical distortions the refractive indices of the dispersed and the continuous phase have to be matched [13]. Recently a review of index matching methods of liquid mixtures and solid materials has been published [14]. When the refractive index of a liquid mixture to a solid material is matched one degree of freedom is necessary. However, in this experiment both the refractive index and the viscosity ratio need to be adjusted. The two degrees of freedom are produced by matching an oil/oil mixture to a water/glucose mixture. The refractive indices of the mixtures are dependent on the mixing ratio of the components as well as on the temperature. Thus, the influence of mixing ratio and temperature is investigated in two separate experiments. First, at a fixed temperature we determine the range in which the refractive indices of both mixtures can be adjusted to one another (Fig. 2). In the second experiment the analysis of the change of viscosity and refractive index with temperature is then used to interpolate the temperature behavior of the refractive index of different mass fractions (see Fig. 4). To reveal the range of matchable indices at a fixed temperature (Fig. 2) the mass fraction $x_B = m_B/(m_A + m_B)$ of the aqueous and the oil mixture is varied and the resulting refractive index is measured. The refractive index range is determined by the oil mixture due to its smaller range (1.4431 - 1.4813). Thus the range of mass fractions of aqueous mixtures is restricted to values between $x_{B,aqueous}(1.4431) = 0.74$ and $x_{B,aqueous}(1.4813) = 0.93$.

For the validation of the above mentioned simulation [2] a droplet impact without immediate breakup is

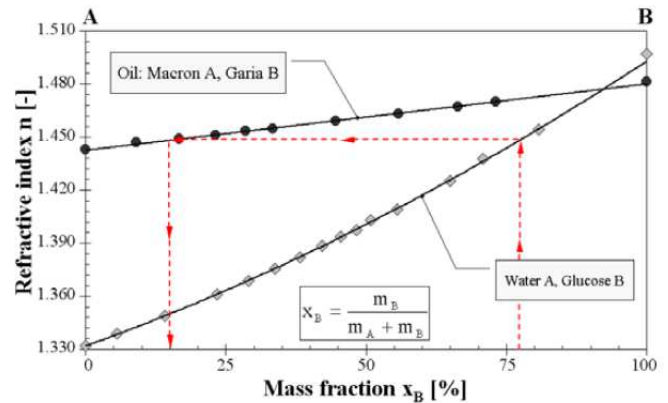


FIG. 2. Refractive index vs. mass fraction x_B at a fixed temperature of $T = 298$ K (25°C). The achievable matching range of refractive indices is restricted due to range of the oil phase. Therefore only aqueous mass fractions between 74% and 93% may be used for index matching.

needed. To produce this kind of impact, rapid drainage of the film between the droplet and the upper surface has to be suppressed. A viscous continuous phase will ensure slow thinning of the film between droplet and top layer. In Fig. 3 the viscosity of the water-glucose mixture is presented as a function of the mass fraction x_B . Referring to the range of matchable refractive indices, possible viscosities of the aqueous phase range between $\eta_{aqueous}(0.74) = 67\text{mPas}$ and $\eta_{aqueous}(0.93) = 934\text{mPas}$. The viscosity of the continuous phase is chosen to be $\eta_{aqueous}(0.77) = 100$ mPas. The corresponding refractive index is according to Fig. 2 $n(x_{B,aqueous} = 0.77) = 1.4482$. Thus, the oil mixture has to have a mass fraction $x_{B,oil} = 0.15$ to match the refractive index. Determining the viscosity of the oil mixture $\eta_{oil}(0.15) \approx 3\text{mPas}$ leads to a viscosity ratio of $\eta_{aqueous}/\eta_{oil} \approx 33$. The refractive index and the viscosity are very sensitive to variations in temperature. This leads to the necessity to predict and compensate for these property changes. Therefore the temperature dependencies of both the viscosity and the refractive index are measured for different mass fractions x_B . However, the temperature correction can be based on an interpolation from a single mass fraction for each mixture, because small changes in the mass fraction do result in an offset of the functional relation, but not in a change of its shape. The data is presented in Fig. 4, showing the graphs for a mass fraction $x_B = 0.10$ of the oil mixture and 0.75 for the aqueous phase. The refractive index is linearly dependent on the temperature while the viscosity depends exponentially. Based on the dependencies provided above, the viscosity of the continuous phase at a desired temperature is chosen and

the required mass fraction x_B of the refractive index matched mixtures are calculated. For other refractive index matching strategies the interested reader is referred

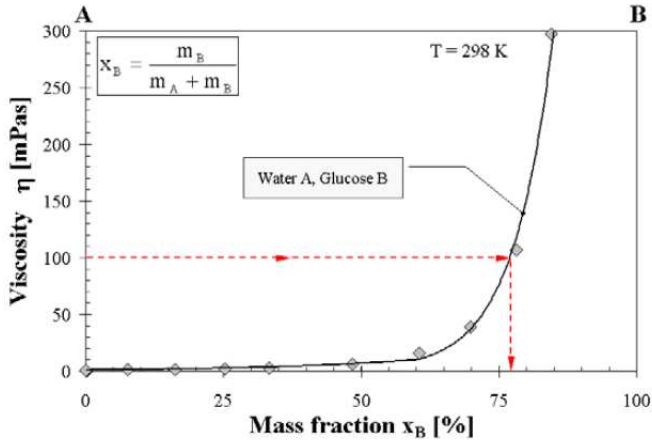


FIG. 3. Dynamic viscosity η vs. mass fraction x_B of glucose B mixed into the water phase A. To avoid rapid droplet breakup, the viscosity of the aqueous mixture is chosen to be 100 mPas. The resulting mass fraction is therefore 77%.

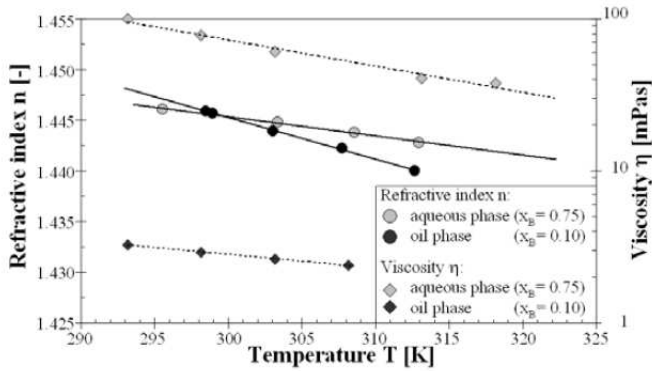


FIG. 4. Refractive index and dynamic viscosity vs. temperature at a fixed mass fraction $x_B = 10\%$ for the oil phase and 75% for the aqueous phase. The relative change of the quantities shown are considered to be independent of the mass fraction for small deviations from the target values.

to [15], [16], [17], [18], [13].

Image processing

The droplet impact is simultaneously observed with two high-speed cameras. One camera records the LIF signal and the second one records the PIV signal. Therefore the processing of the captured images from the experiments consists of two parts: First, extraction of droplet location and shape (from the LIF data) and second, measurement of the fluid velocity field (from the PIV data). The PIV data is used to study the possibility of optimizing the time separation between two correlated images.

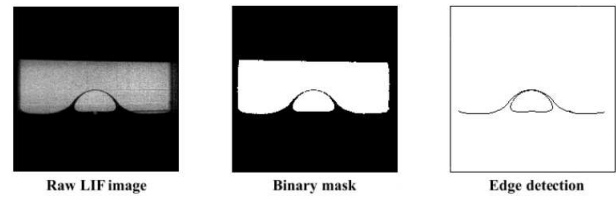


FIG. 5. Processing of the LIF images: A threshold filter is applied to the raw LIF image. The resulting binary mask will provide the position of the interfaces using an edge detection method (Sobel).

LIF processing

The evaluation of the LIF images is performed in Matlab 7.0. First, each image is converted to a binary bitmap using a threshold filter (see Fig. 5). The threshold value is a fixed value for the entire image series. From the resulting binary images, the following parameters are extracted:

- position of the interface
- the droplet top position
- the center of area
- the bottom of the droplet
- horizontal and vertical diameter

Furthermore, using an edge detection method (Sobel), the shape of both the droplet and the deforming interface is captured. This information will also be used to identify the different phases in the PIV results.

PIV processing

The raw PIV images are pretreated for the analysis in chapter 3. Due to extinction the intensity of the laser light sheet is not uniform over the measurement area. These intensity gradients of the light sheet can be removed from the raw images by applying a non-linear filter, which subtracts the sliding minimum from the PIV image. The spatial sliding minimum filter computes the minimum intensity in a neighborhood of pixels. This is done for efficiency using a sliding minimum filter operation. The spatial sliding minimum is then subtracted to remove background noise. The filter length is chosen much larger than the particle image diameter, in order to maintain the particle information [19]. The PIV calculation of vector fields is performed with in-house software by using cross-correlation with a decreasing interrogation window size starting with 3232 pixels to estimate the pre-shift for two subsequent correlations using 1616 pixel interrogation windows with 50% overlap. The obtained vector field is subsequently post-processed using

a universal outlier detection algorithm [20] to label spurious vectors.

EVALUATION

During a short period of time of approximately 2 seconds, the rising droplet approaches the interface, impacts into the oil top layer and oscillates around its equilibrium state. Coalescence of the droplet with the top-layer is prevented by a thin film of the continuous phase. Only after several minutes, the thin film is drained and the droplet merges with the top layer. During the impact the velocity magnitude changes in time and space (i.e. acceleration/ deceleration due to the oscillation and velocity gradients due to strong local fluid motion). A fixed time interval between the correlated particle images throughout the impact sequence will lead to inaccuracies, either in the parts of the measurement sequence with low or with high velocities. This error depends on the chosen length of the time interval. In order to increase the accuracy of the high-speed PIV temporal and spatial variations of the velocity within the sequence have to be taken into account. Since PIV is based on cross-correlation, a measure for valid correlations is the signal-to-noise ratio (SNR), which is given by the ratio between the highest correlation peak to the second highest. An excellent SNR can be achieved using the smallest time interval possible. However the measured particle image displacements will be in the range of the measurement accuracy of the PIV system. Applying a long time interval results in sufficient SNR for small particle image displacements, but causes decorrelation in faster parts of the vector field. Thus an optimum has to be found to combine a high velocity dynamic range (VDR) with a high SNR.

Analysis of the vector fields

In order to search for a quantity that indicates the quality of a PIV evaluation the sequence of a single droplet impact event is evaluated several times, each time increasing the time interval $\Delta t_{PIV} = k \cdot \Delta t_{cam}$, with Δt_{cam} being the time interval between consecutive pictures. For $\Delta t_{PIV}/\Delta t_{cam} = 4$ an example is given in Fig. 6 for a time t_0 during a sequence. As a first indication of the quality of a PIV evaluation the percentage of outliers inside each vector field of the above described data sets is calculated. The number of outliers can be regarded as a measure of the decorrelation of the PIV signal. According to Keane and Adrian [21] an amount of spurious vectors of less than 5% in a PIV measurement is considered to be acceptable. In Fig. 7 the development of the outliers in the computed vector fields is shown as a function of time and length of the time interval between correlated particle images. Each axis is normalized with

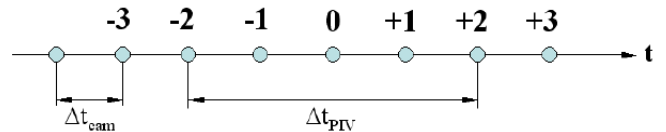


FIG. 6. Adjustment of time interval Δt_{PIV} : In this example three images are skipped between the correlated images. This results in an effective separation time $\Delta t_{PIV} = 4\Delta t_{cam}$ between frames $n = -2$ and $n = +2$ for the time t_0 .

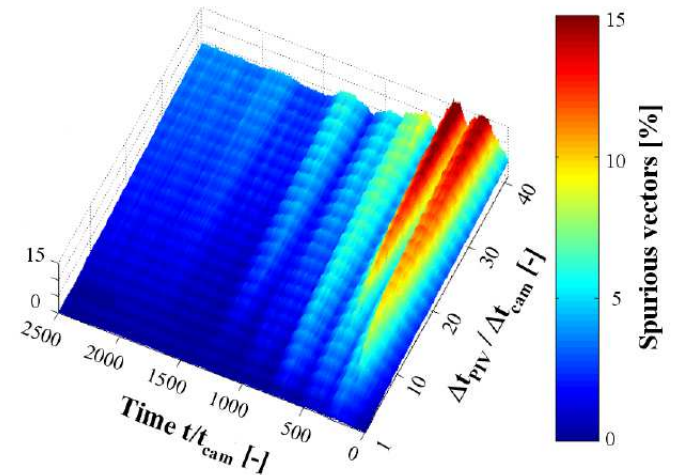


FIG. 7. Survey of percentage of spurious vectors over time t/t_{cam} and time interval t_{PIV}/t_{cam} .

the recording interval Δt_{cam} . The oscillation of the outlier amplitude corresponds to the oscillating movement of the droplet during the impact. Increasing time interval Δt_{PIV} results in a magnification of the amplitude of the oscillation (i.e. an increase of spurious vectors).

A comparison of the occurrence of outliers for three different time intervals (consecutive, $3\Delta t_{cam}$, $6\Delta t_{cam}$) reveals important similarities. All maxima occur at the same time instant. The first maximum is located at $t/t_{cam} = 212$ and will be used in the following as a reference for comparison.

Determination of an indicator

In order to obtain a more relevant link to the occurrence of spurious vectors the origin of the outliers with respect to the evolving flow needs to be detected. Possible reasons for a failure of the cross correlation are spatial and temporal velocity gradients. Results of a more detailed investigation are given in Fig. 9. The maximum absolute displacements of the vector fields are used as an indicator for spatial velocity gradients. The temporal derivative of this quantity serves as a qualitative indica-

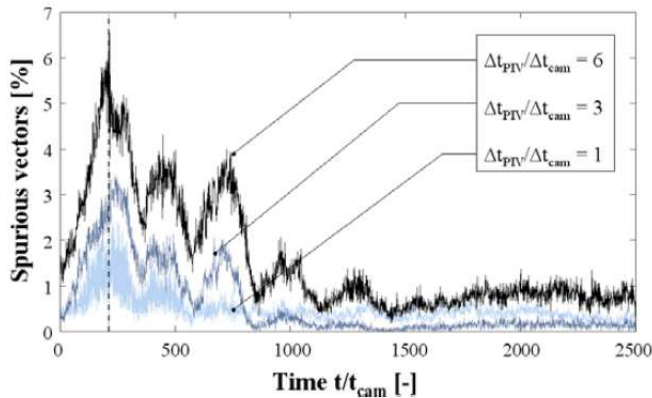


FIG. 8. Percentage of Spurious vectors of the time series using time interval with $t_{PIV}/t_{cam} = 1, 3$ and 6 respectively.

tor for temporal velocity gradients. With respect to the first maximum of the outlier development $t/t_{cam} = 212$, it can be shown that temporal velocity gradients (i.e. temporal derivative of the maximum particle image displacement) are not the cause of the occurring outliers. In fact the spatial gradients (i.e. maximum particle image displacement) are considered to be the cause of the spurious data. A good indicator for spatial velocity gradients is given by the standard deviation (RMS) of all displacements within a vector field. This quantity increases with increasing differences in the spatial distribution of velocities. In Fig. 9 it can be seen that the maximum of the RMS value coincides with the maximum of spurious vectors. Thus, this quantity will be used as a criterion to optimize the time interval Δt_{PIV} between two correlated images.

Optimization

After identifying the RMS value of the vector fields as an indicator for the occurrence of outliers, a connection is needed between the change of RMS to the time interval between correlated particle images. Thus, an investigation of the RMS of the mean particle image displacement over time and increasing time interval Δt_{PIV} is shown in Fig. 10.

Fig. 10 reveals that the value of the RMS scales (obviously) linearly with the time interval. Normalizing the RMS developments with the time interval shows that the evolution of the standard deviation throughout the times series is self-similar. Thus, fitting a polynomial with a least-square fit to the normalized RMS of the displacements enables computation of the change of the standard deviation as a continuous 2-D function with respect to the impact time frame t and time interval Δt_{PIV} . To indicate the resemblance of the fit, Fig. 10 a.) shows the part of the 2-D function which represents the time

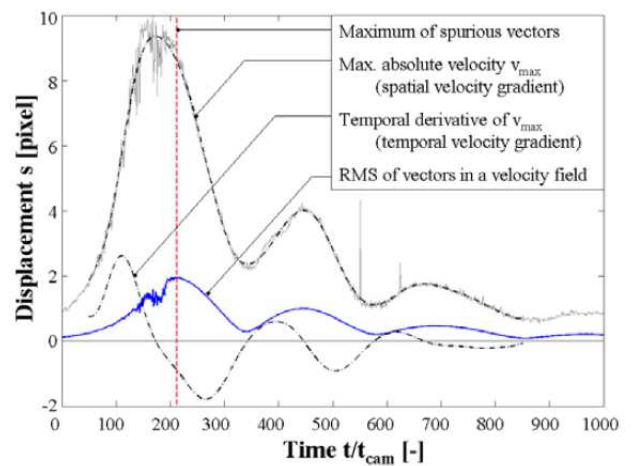


FIG. 9. The maximum of absolute particle image displacement as an indicator for spatial velocity gradients is compared to the change of displacement as an qualitative indicator for the temporal velocity gradients. The maximum of the RMS of the vector fields coincides with the occurrence of the maximal number of spurious vectors and will thus be used in the following for the optimization.

interval $\Delta t_{PIV} = 11 \cdot \Delta t_{cam}$. The deviation of the fit to the data is caused by decorrelation. Large displacements result in a loss of pairs in time. If that occurs, closer particle image pairs are correlated and lead thus to smaller displacements (Fig. 10 b.)). In order to avoid decorrelation the optimized time interval needs to be adjusted such that the resulting RMS of displacements do not indicate the occurrence of spurious vectors. However, the time interval has to be sufficiently long to keep the measured displacements outside the measurement accuracy of the PIV system. Fig. 10 c.) shows the RMS development of the data set for $\Delta t_{PIV}/\Delta t_{cam} = 1$, i.e. consecutive image frames and therefore serves as lower boundary for the optimization. The upper limit is determined by the occurrence of spurious vectors. Setting the target RMS of the displacements to a constant value (Fig. 10 d.)) results in a contour line of the 2-D fit and provides the necessary functional dependence between the impact time frame t and the time interval Δt_{PIV} . In Fig. 11 the dependence of the time interval of the correlation Δt_{PIV} and the impact time t/t_{cam} is plotted. Sections in the sequence where the

fluid is moving fast have a short time interval (see $t/\Delta t_{cam} = 212$, i.e. small $\Delta t_{PIV}/\Delta t_{cam}$). When the liquid moves slowly the displacements will be calculated with a large Δt_{PIV} ($t/\Delta t_{cam} = 850$, i.e. large $\Delta t_{PIV}/\Delta t_{cam}$). An optimized time series of velocity data is generated by choosing the evaluation with the optimal time interval according to Fig. 11 for each individual time step during the sequence. For that purpose the continuous contour line of optimal time intervals in Fig. 11 needs to be transferred in discrete integer val-

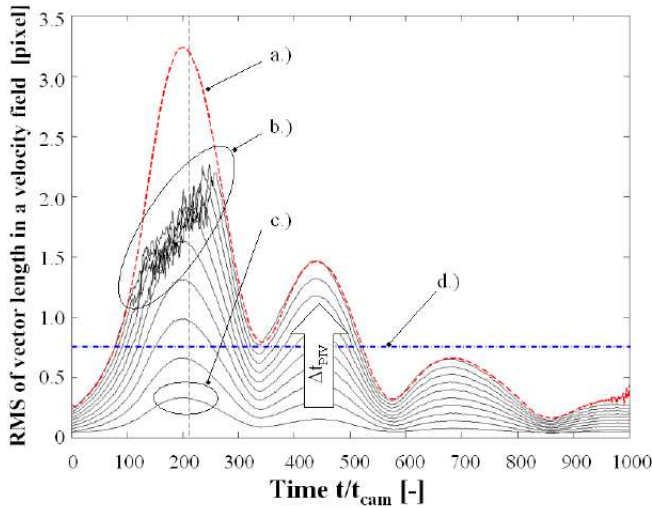


FIG. 10. Oscillation of the RMS of the particle image displacement (varied time interval t_{PIV}/t_{cam} for each graph 1 up to 11), influence of spurious vectors and threshold chosen.

ues. All measured displacements are normalized with their original time interval Δt_{PIV} .

RESULTS AND DISCUSSION

This chapter is divided into two parts. First, the result of the optimization is presented and discussed. Second, a brief comparison with the corresponding numerical simulation [2] is given.

Optimization

Due to the discrete nature of the variability of the time interval the rounding procedure used does not exactly produce a constant fraction of spurious vectors throughout the time series. In Fig. 12 the result for the spurious vectors of the optimized series is compared to the spurious vector occurrence for a series with fixed time separations of $\Delta t_{PIV}/\Delta t_{cam} = 1$ and 6 respectively. The optimized time series shows that the amount of spurious vectors is reduced below the limit of 5%. The time varying behavior on the flow conditions cannot be recognized any longer and the percentage of spurious vectors is limited to an almost constant value between 1.2 and 4.4% (dashed lines).

Since the vorticity is obtained by differentiation it is sensitive to spurious vectors. Thus, to show differences between a constant PIV evaluation time interval and the above presented optimized approach, vorticity plots are compared. In Fig. 13 the change in length of the time interval $\Delta t_{PIV}/\Delta t_{cam}$ is plotted vs. the impact time scale $t/\Delta t_{cam}$. In order to compare the time scale used

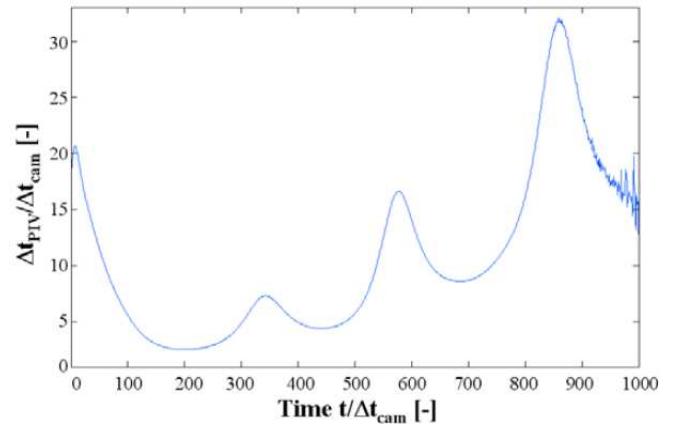


FIG. 11. Time interval $\Delta t_{PIV}/\Delta t_{cam}$ adjusted to the different parts of the impact sequence.

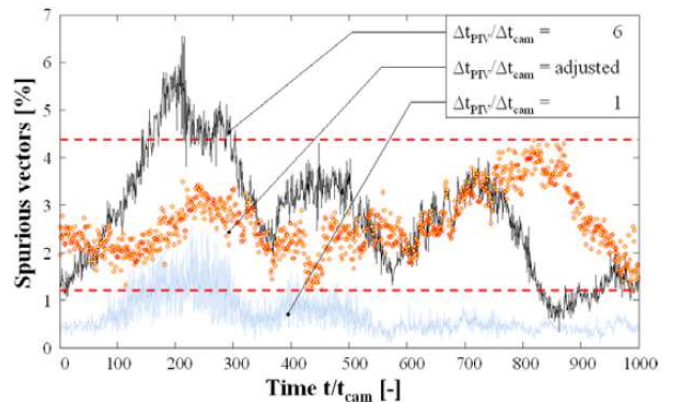


FIG. 12. Percentage of spurious vectors with adjusted time interval $\Delta t_{PIV}/\Delta t_{cam}$ compared to the results of a the series evaluated with $\Delta t_{PIV}/\Delta t_{cam} [1, 6]$.

by [1] with this experiment a second time scale t/t_i is introduced.

Here $t_i = D/U_i$ represents an impact velocity time scale based on the droplet diameter D and the impact velocity U_i of the droplet. The dashed line represents a PIV evaluation using a constant time interval $\Delta t_{PIV} = 6\Delta t_{cam}$. The length of constant time interval is chosen to be the same as in [1]. To show differences in the resulting vorticity fields three time instances t_1 , t_2 and t_3 are compared. The positions represent part of an oscillation between an upper and a lower turning point of the droplet. At time $t/t_i = 3.1$ the droplet starts to move from the lower turning point. When the maximum velocity is reached, the time interval is minimal (time instant t_1) in Fig. 13). With time t_2 at $t/t_i = 4.9$ in Fig. 13 an intermediate position is chosen between the maximal fluid movement and the upper turning point t_3 at $t/t_i = 5.3$. The aspect ratio of the droplet has a first minimum at $t/t_i = 1.9$ (t_4 in Fig. 13). This time instant

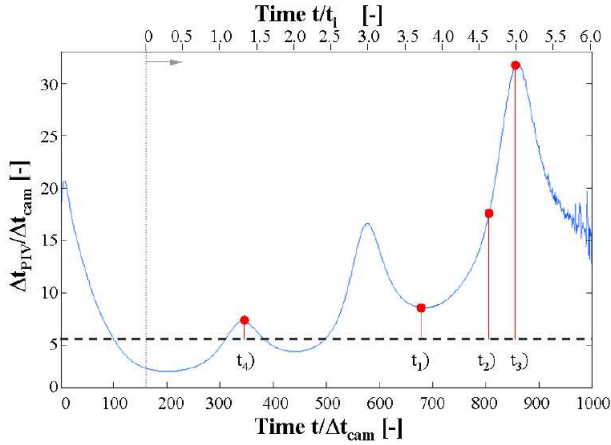


FIG. 13. The optimized time interval is plotted in comparison to a constant time interval. t_1 , t_2 and t_3) respectively show the time instants at which vorticity plots of both approaches are compared. On t_4) a minimum of the aspect ratio occurs. This time instant is chosen for a comparison with the vorticity features discovered by [1]. For convenience the time scale presented by [1] is introduced, where $t_i = D/U_i$ represents an impact velocity time scale based on the droplet diameter D and the impact velocity U_i of the droplet.

will be used to compare the physical features of this flow with the results published by [1].

From the data sets in Fig. 14 (t_1 , t_2 , t_3) the vorticity plots in Fig. 15 are computed. For all three time instants the evaluation using the constant time interval $\Delta t_{PIV}/\Delta t_{cam} = 6$ is shown in the top row and the optimized time interval is printed below. The deviation of fixed and variable time interval increases with time t/t_i from a) to c) due to the reduction of velocity from a local maximum a) to the upper dead point c) of the oscillation cycle. In Fig. 14 a) the time interval differs by a factor of 1.6 due to the higher velocity of the flow. The vorticity plot of the adjusted time interval contains less noise and the flow features are represented more clearly than in the constant approach. The symmetry is more explicit in the optimized evaluation. Differences in terms of noise are most obvious in the intermediate example in Fig. 14 b) when the flow slows down towards the upper dead point. The optimization has achieved reduction of noise while the features of the flow are captured as well as in the constant approach. The symmetry plane is more expressed in the optimized case. Due to the minimal movement in the upper dead point (Fig. 14 c)) the magnitude of vorticity in both evaluations is smaller than in the first examples. However the noisier appearance of the vorticity due to the constant time interval is still visible in comparison with the optimization. The symmetry of the flow is more expressed in the adjusted approach.

The drop internal circulation at a characteristic instant during the impact of the droplet is shown in Fig. 15

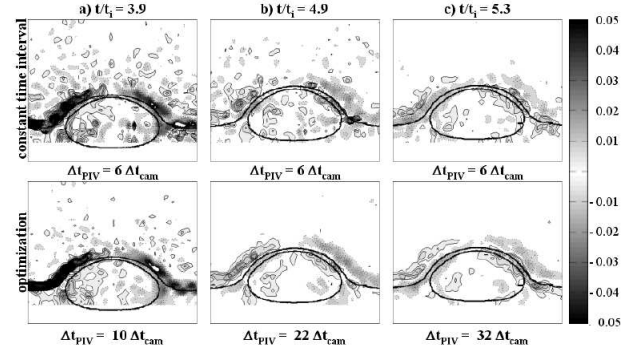


FIG. 14. Comparison of PIV evaluation with a constant time interval $\Delta t_{PIV}/\Delta t_{cam} = 6$ (top row) with the optimized approach (bottom row). The time instants shown agree with the time instances t_1 , t_2 and t_3) in Fig. 13. Positive vorticity values are represented by solid lines and negative by dashed lines. Due to the optimization the vorticity plots are less noisy and more symmetric

a) to c). Based on these plots, the physical features of the experiments of Mohamed-Kassim and Longmire [1] are compared to this study. In Fig. 15 b) and c) two vorticity plots of [1] with a viscosity ratio of $\lambda = 0.14$ and $\lambda = 0.33$ respectively are shown. The time instant chosen is $t/t_i = 1.4$ due to the occurrence of the first minimum of the droplet aspect ratio. In the present study (Fig. 15 a)) the first minimum of the aspect ratio occurs at a later time instant $t/t_i = 1.9$ and the viscosity ratio $\lambda = 0.03$ is smaller. For the convenience of comparison the vorticity plot of this study is rotated upside down. The remainder of the leading vortex ring inside the droplet is visible in all three examples. The features of the counter rotating vortex induced by the earlier impinging wake can also be found in all vorticity plots shown. The drainage of the film between the droplet and the interface is slow due to the considerably lower viscosity ratio $\lambda = 0.03$ (i.e. larger ambient viscosity) in Fig. 15 a). A layer of ambient liquid is still draining from the liquid bridge while the first minimum of the aspect ratio is reached. The remaining parts of the leading vortex inside the drop are decelerated by this viscous film and result in an area of counter rotating vorticity at the surface of the droplet. Due to a limited field of view not the full area of interest upstream of the droplet position d3 can be seen.

Comparison of simulation and experiment

In this section, results of the experimental investigation are compared to results of the numerical study by Coyajee et al. [2]. In the numerical study, drop impact on an interface is simulated using the MCLS method [10], a Finite difference/ Front-capturing method. To compute fluid motion, the Navier- Stokes equations are

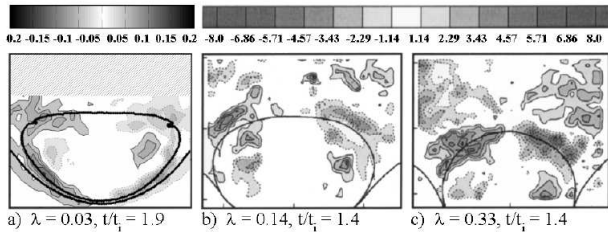


FIG. 15. The vorticity flow features published by Mohamed-Kassim and Longmire [1] with two different viscosity ratios $\lambda = 0.14$ and 0.33 at the impact time $t/t_i = 1.4$ compared with the according result of the present study ($\lambda = 0.03$, $t/t_i = 1.9$). Positive vorticity values are represented by solid lines and negative by dashed lines.

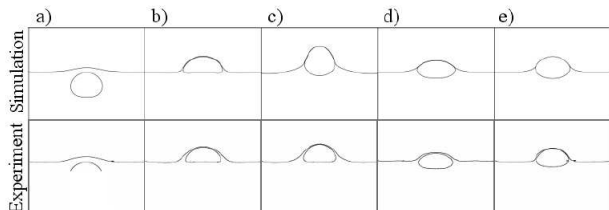


FIG. 16. Qualitative comparison of the computed (top) and the LIF measurement of the Droplet shape (bottom).

solved on a fixed Cartesian grid, taking into account different viscosity and density in each phase and surface tension forces on the interface between the phases. The interface is tracked with a combined Level-Set/Volume-of-Fluid method. For further details on the computational method, we refer to [9], [10] and [2].

LIF results

In Fig. 16, contour lines of the droplet and the top layer interface are compared at different instances during the impact event. The upper row shows the numerical results, while the bottom row represents processed images of the experimental LIF data. Note that the experimental data are obtained within a limited field of view and therefore only part of the droplet is visible in the first frame. Fig. 16 reveals qualitative agreement of the droplet and interface deformation during drop impact. However, in the simulation the droplet is found to penetrate further into the top layer (image c). In addition, the simulation shows immediate drainage of the bridging gap between the droplet and the interface of the top layer. Due to a limited number of computational cells available this thin film is not resolved in the simulation.

For quantitative comparison of experiment and simulation three parameters are chosen:

- vertical position of the droplet center of mass,

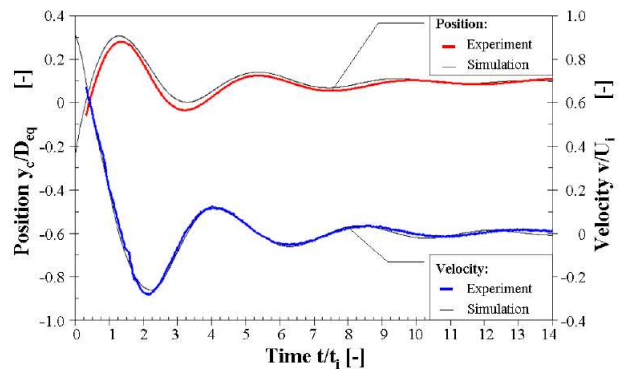


FIG. 17. Center point position and velocity of the simulation (thin line) is compared to the experimental results (thick line).

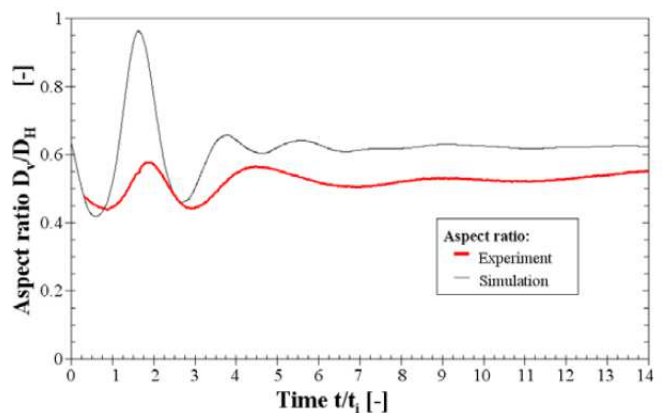


FIG. 18. Comparison of the aspect ratio of the droplet during the impact as obtained from the experimental and numerical results.

- vertical velocity of the droplet center of mass,
- droplet aspect ratio (ratio of the horizontal and vertical droplet diameter).

Time evolution of the droplet position and velocity is presented in Fig. 17 for both the experiment and simulation. The left vertical axis of Fig. 17 shows the droplet position, while the right vertical axis shows the droplet velocity. The simulation of the droplet center point matches the measurement data closely. In Fig. 18, time evolution of the droplet aspect ratio is displayed. Comparison of simulated and experimental results shows good qualitative agreement, but the magnitude of the droplet deformation is too large in the numerical simulation. The difference between the numerical and experimental results may be explained from the importance of the thin film, which is not resolved in the numerical simulation. In the current drop impact experiment the viscosity of the continuous phase is much larger than the viscosity of the droplet phase. As a result, a considerable film of the continuous phase persists in the gap

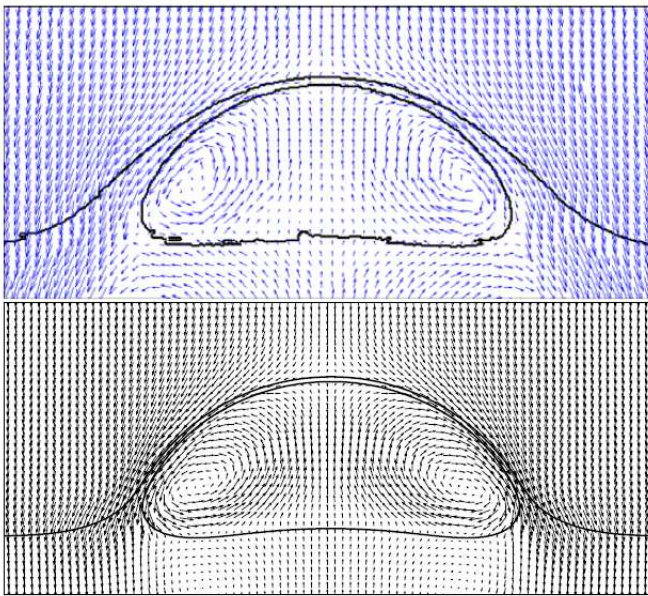


FIG. 19. Interfaces and velocity vectors at maximum D_w/D_h of the experiment (top) and the simulation (bottom).

between the droplet and the top layer interface during the impact event. In the study of Mohamed-Kassim & Longmire, the viscosity ratio is much closer to unity (Tab. 1) and the thin film between the droplet and the interface is much smaller (Fig. 2,3 and 6 of [1]). Preliminary simulations using the experimental parameters of Mohamed-Kassim & Longmire show much better quantitative agreement between numerical and experimental results for the droplet deformation.

PIV results

In Fig. 19, flow fields of experiment and simulation are compared by displaying velocity vectors over a cross section of the domain. The time instant of each image is $t/t_i = 0.9$, where D_w/D_h has a maximum. Qualitative agreement of the flow patterns is found, e.g. the similarly situated center of rotation inside the droplet, the impinging wake and the jet caused by the draining film. The thickness of the film in the simulation is smaller and almost constant along the interface of the droplet.

The vorticity plots shown in Fig. 20 are derived from the velocity fields presented above (Fig. 19). The upper image represents the experimental data, the lower shows the result of the simulation. Most flow features shown by the experiment can also be found in the results of the DNS. The resemblance of the vortex ring inside the simulated droplet and the measurement is good and the vorticity due to the impinging wake matches. Also the shear field of the drained fluid from the film is present in both the experiment and simulation.

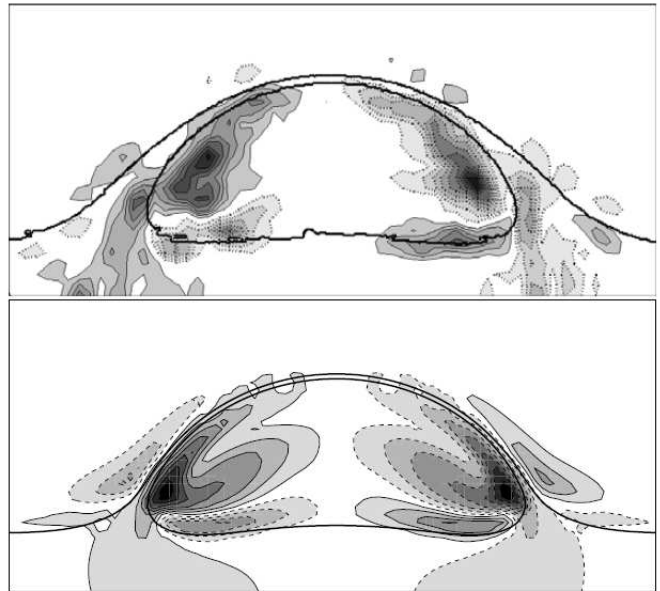


FIG. 20. Interfaces and vorticity contour levels at maximum D_w/D_h of the experiment (top) and the simulation (bottom).

CONCLUSION

This paper describes an approach to optimize the evaluation quality of highspeed PIV. Spatial and temporal velocity gradients in the flow are the cause

of variations in the quality of the PIV result. Large time separation result in decorrelation with an increase of spurious vectors as a result. A small time separation provides a very high reliability (very few spurious vectors) but are not meaningful because the measured particle image displacement is found to be in the range of measurement error (0.1 pixel). Taking into account the observed flow conditions, an adjustable time separation between two correlated images is proposed. In order to find an optimal time separation within a high-speed sequence the fraction of spurious vectors is used to monitor the data quality. Based on an analysis of the flow properties with standard evaluation methods the RMS of the particle image displacement of the vector field is found to be an indicator for spatial gradients in the considered flow. Keeping the RMS constant over time, we achieved a constant fraction of spurious data and thus identified the largest possible time separation. This maximized the VDR throughout the measurement sequence. Further work has to be done in order to explore the possibility to use an adjustable separation time not only related with entire images but also for each interrogation window within an image frame. In this manner it will be possible to calculate vector fields with an optimal particle image displacement throughout the whole vector field series and within each field. The comparison of the experimental data presented in this study with numerical

calculations presented by [2] reaches at this stage a basic level. The parameters extracted from the experiment can only provide general statements about the capability of the simulation to predict the flow pattern. The qualitative and quantitative parameters chosen show a reasonable capture of droplet shape and good results for the simulation of the center point motion and velocity. The difference in aspect ratio may be partially explained with the fast drainage of the thin film of viscous fluid in the simulation. However, judging the capability of the numerical simulation may be topic of future detailed investigation of the now improved PIV data set.

* U.Miessner@tudelft.nl

- [1] Z. Mohamed-Kassim and E. Longmire, *Physics of Fluids* **15**, 3263 (2003)
- [2] E. Coymjee, R. Delfos, H. Slot, and B. Boersma, *Direct and Large-Eddy Simulation VI*, 329(2006)
- [3] R. Delfos, C. Poelma, P. Poesio, R. Kaijen, and J. Westerweel, *Proceedings of the APS - (Division Fluid Dynamics) meeting*(2004)
- [4] R. Delfos, C. Poelma, R. Kaijen, and J. Westerweel, *Proceedings of the 6th International Symposium on Particle Image Velocimetry*, 1(2005)
- [5] K. J. Westerweel J, Stanislas M, 17(2004)
- [6] R. R. Nerger D, Kähler CJ, *Lasermethoden in der Strömungsmesstechnik* **10** (2003)
- [7] R. Hain and C. Kähler, *6th International Symposium on Particle Image, Pasadena*(2005)
- [8] Expressed as the signal-to-noise ratio (SNR), usually obtained from the correlation peak height.
- [9] S. Van der Pijl, *Computation of bubbly flows with a Mass-Conserving Level-Set method*, Ph.D. thesis, Delft University of technology (2005)
- [10] S. Van der Pijl, A. Segal, C. Vuik, and P. Wesseling, *International journal for numerical methods in fluids* **47**, 339 (2005)
- [11] R. Lindken and W. Merzkirch, *Experiments in fluids* **29**, 194 (2000)
- [12] C. Willert, *Measurement science and technology* **8**, 1465 (1997)
- [13] A. Zachos, M. Kaiser, and W. Merzkirch, *Experiments in fluids* **20**, 229 (1996)
- [14] P. Miller, K. Danielson, G. Moody, A. Slifka, E. Drexler, and J. Hertzberg, *Experiments in fluids* **41**, 375 (2006)
- [15] R. Budwig, *Experiments in fluids* **17**, 350 (1994)
- [16] T. Narrow, M. Yoda, and S. Abdel-Khalik, *Experiments in fluids* **28**, 282 (2000)
- [17] T. Nguyen, Y. Biadillah, R. Mongrain, J. Brunette, J. Tardif, and O. Bertrand, *Journal of biomechanical engineering* **126**, 529 (2004)
- [18] M. Cui and R. Adrian, *Experiments in fluids* **22**, 261 (1997)
- [19] R. Lindken, J. Westerweel, and B. Wieneke, *Experiments in fluids* **41**, 161 (2006)
- [20] J. Westerweel and F. Scarano, *Experiments in Fluids* **39**, 1096 (2005)
- [21] R. Keane and R. Adrian, *Measurement Science and Technology* **1**, 1202 (1990)